



Publication Year	2018
Acceptance in OA@INAF	2021-04-21T13:38:31Z
Title	Massive $70 \frac{1}{4} M_{\odot}$ quiet clumps - II. Non-thermal motions and star formation?
Authors	TRAFICANTE, ALESSIO; Fuller, G. A.; Smith, R. J.; Billot, N.; Duarte-Cabral, A.; et al.
DOI	10.1093/mnras/stx2672
Handle	http://hdl.handle.net/20.500.12386/30831
Journal	MONTHLY NOTICES OF THE ROYAL ASTRONOMICAL SOCIETY
Number	473

Massive 70 μm quiet clumps – II. Non-thermal motions driven by gravity in massive star formation?

A. Traficante,^{1,2★} G. A. Fuller,¹ R. J. Smith,¹ N. Billot,³ A. Duarte-Cabral,⁴
N. Peretto,⁴ S. Molinari² and J. E. Pineda⁵

¹Jodrell Bank Centre for Astrophysics, School of Physics and Astronomy, University of Manchester, Oxford Road, Manchester M13 9PL, UK

²IAPS – INAF, via Fosso del Cavaliere, 100, I-00133 Roma, Italy

³Instituto de Radio Astronomía Milimétrica, Avenida Divina Pastora, 7, Local 20, E-18012 Granada, Spain

⁴School of Physics and Astronomy, Cardiff University, Queens Buildings, The Parade, Cardiff CF24 3AA, UK

⁵Max-Planck-Institut für extraterrestrische Physik (MPE), Gießenbachstrasse 1, D-85741 Garching, Germany

Accepted 2017 October 11. Received 2017 October 11; in original form 2017 May 23

ABSTRACT

The dynamic activity in massive star-forming regions prior to the formation of bright protostars is still not fully investigated. In this work, we present observations of $\text{HCO}^+ J = 1-0$ and $\text{N}_2\text{H}^+ J = 1-0$ made with the IRAM 30 m telescope towards a sample of 16 *Herschel*-identified massive 70 μm quiet clumps associated with infrared dark clouds. The clumps span a mass range from 300 to 2000 M_\odot . The N_2H^+ data show that the regions have significant non-thermal motions with velocity dispersion between 0.28 and 1.5 km s^{-1} , corresponding to Mach numbers between 2.6 and 11.5. The majority of the 70 μm quiet clumps have asymmetric HCO^+ line profiles, indicative of significant dynamical activity. We show that there is a correlation between the degree of line asymmetry and the surface density Σ of the clumps, with clumps of $\Sigma \gtrsim 0.1 \text{ g cm}^{-2}$ having more asymmetric line profiles, and so are more dynamically active, than clumps with lower Σ . We explore the relationship between velocity dispersion, radius and Σ and show how it can be interpreted as a relationship between an acceleration generated by the gravitational field, a_G , and the measured kinetic acceleration, a_k , consistent with the majority of the non-thermal motions originating from self-gravity. Finally, we consider the role of external pressure and magnetic fields in the interplay of forces.

Key words: turbulence – stars: evolution – stars: formation – stars: kinematics and dynamics – stars: massive – radio lines: stars.

1 INTRODUCTION

Pioneering studies of star-forming regions showed a significant contribution from the ambient interstellar medium (ISM) turbulence in dictating the properties of clouds. This was first summarized in the Larson linewidth–size relation $\delta v \propto R^\Gamma$, with $\Gamma = 0.38$ (Larson 1981). Later this value was modified to $\Gamma = 0.5$, consistent with early observations of giant molecular clouds (GMCs) that show that GMCs have all similar mass surface densities, Σ , and turbulence is ubiquitous in the ISM (e.g. Solomon et al. 1987; Heyer & Brunt 2004). The exponent $\Gamma = 0.5$ is expected if the ISM is modelled as a turbulent fluid dominated by shocks (McKee & Ostriker 2007, and references therein) and simulations confirm that GMCs and their embedded massive clumps are shaped by supersonic motions and follow the Larson relationship with $\Gamma = 0.5$ (e.g. Padoan & Nordlund 2002; Field, Blackman & Keto 2008).

More recently, the study of Heyer et al. (2009, hereafter H09) questioned the Larson relation and showed that the quantity $\sigma/R^{0.5}$ is not a constant of the clouds. H09 used data from the Boston University-FCRAO Galactic Ring Survey of $^{13}\text{CO } J = 1-0$ emission (Jackson et al. 2006) to revise the study of the GMCs done by Solomon et al. (1987) using the $^{12}\text{CO } J = 1-0$ emission. The latter is a tracer of low-density gas, which rapidly becomes optically thick within the denser regions of the GMCs. The H09 analysis shows that the average mass surface density Σ of the clouds is not constant, and that $\sigma/R^{0.5}$ increases as a function of Σ , which we will refer to as the ‘Heyer relation’.

It is unclear, however, how the Heyer relation may or may not cascade down to the scales of clumps and cores. While inside low-mass cores the turbulence seems to dissipate down to thermal levels (i.e. following the standard Larson relation $\sigma \propto R^{0.5}$; Fuller & Myers 1992), there are some indications that this does not happen in massive star-forming clumps and cores (Ballesteros-Paredes et al. 2011). For instance, combining the data from H09 with a sample of massive clumps identified in infrared dark clouds (IRDCs) from Gibson et al. (2009), Ballesteros-Paredes et al. (2011)

* E-mail: alessio.traficante@iaps.inaf.it

interpreted the Heyer relation as ‘universal’, from GMCs down to clump scales. In the Ballesteros-Paredes et al. (2011) model, the observed large velocity dispersions are driven by the non-thermal motions in the collapsing clouds and cloud fragments in a hierarchical and chaotic fashion (see also Vázquez-Semadeni et al. 2009; Ibáñez-Mejía et al. 2016).

In an alternative view, the observed non-thermal motions in massive regions could be attributed to increasing internal turbulence required to maintain equilibrium and slow down the otherwise fast collapse, as predicted by the turbulent core model of massive star formation (McKee & Tan 2003).

Whether the observed non-thermal motions in high-mass clumps and cores are in any way related to a surface density threshold, Σ_t , below which massive star formation cannot occur (Kauffmann, Pillai & Goldsmith 2013), or if Σ_t even exists, are still open questions.

Models suggest different values for Σ_t depending on the contribution of the magnetic fields, with Tan et al. (2014) suggesting $\Sigma_t = 0.1 \text{ g cm}^{-2}$ in the presence of magnetic fields, and Krumholz & Tan (2007) deriving $\Sigma_t = 1 \text{ g cm}^{-2}$ for non-magnetized regions. Recent surveys of massive star-forming clumps show that they span a range of surface densities, with possible Σ_t values ranging from $\Sigma_t \cong 0.05 \text{ g cm}^{-2}$ (e.g. Urquhart et al. 2014) to $\Sigma_t \cong 0.1\text{--}0.2 \text{ g cm}^{-2}$ (e.g. Tan et al. 2014; Traficante et al. 2015).

In this work, we discuss the results from a study of 70 μm quiet clumps, focusing on the properties of their non-thermal motions. Since these high surface density objects are probable precursors to massive stars but are as yet unaffected by stellar feedback, they are ideal candidates for the study of the dynamical state of the initial conditions for massive star formation.

This paper is structured as follows: in Section 2, we describe the observations of a sample of 16 clumps identified in the IRDC survey of starless and proto-stellar clumps of Traficante et al. (2015) that we followed up with the IRAM 30 m telescope¹ to trace the gas kinematics. In Section 3, we describe the properties of the clumps used in this work and derived from dust and gas observations (Section 3.1), and we investigate the clump dynamics and the degree of line asymmetry in the HCO^+ spectra (Section 3.2). In Section 4, we explore the clump stability using a classical virial analysis and using a formulation that compares the acceleration driven by different forces. In Section 5, we explore how the relation between the gravitational acceleration and the non-thermal motions varies from GMCs to massive clumps and cores, combining our data with results from the literature (Section 5.1). We also explore the effect of including an external pressure (Section 5.2) and magnetic fields (Section 5.3) on the force balance. Finally, in Section 6 we summarize our results and present our conclusions.

2 OBSERVATIONS

In this work, we focus on the properties of the non-thermal motions of a sample of 16 clumps selected to be 70 μm quiet, have a surface density $\Sigma \geq 0.05 \text{ g cm}^{-2}$, a mass of $300 \leq M \leq 2000 M_\odot$ and a low luminosity-to-mass ratio $L/M < 0.3$. A comprehensive description of the clump properties estimated from the dust continuum and a more extensive analysis of the molecular line data are given in Traficante et al. (2017, hereafter PI).

¹ IRAM is supported by INSU/CNRS (France), MPG (Germany) and IGN (Spain).

These clumps are located at distances ranging between $3.5 \leq d \leq 5.8 \text{ kpc}$ and have been observed with the IRAM 30 m telescope using N_2H^+ (1–0), HNC (1–0) and HCO^+ (1–0) emission lines. The observations were carried out in 2014 June under the project number 034-14 in good weather with system temperatures between 92 and 162 K. Each source was mapped in on-the-fly mode to cover a $2 \text{ arcmin} \times 2 \text{ arcmin}$ wide region with typical rms noise levels of $0.13 \leq \sigma \leq 0.32 \text{ K}$ in each 0.2 km s^{-1} spectral channel. The telescope pointing was checked every 2 h and the pointing error is estimated to be $< 3 \text{ arcsec}$. At the frequency of these transitions, the beam size of the telescope is $\cong 27 \text{ arcsec}$, corresponding to $\cong 0.6 \text{ pc}$ at a distance of 4.8 kpc, the average distance of these clumps (PI).

3 RESULTS

3.1 Clump physical properties

To investigate the physical properties of our clumps, we make use of the mass surface density estimated from the Hi-GAL data (PI). We also use the emission from N_2H^+ , an optically thin tracer of quiescent gas (Vasyunina et al. 2011) not strongly affected by infall or outflow motions, to measure the systemic velocity of the clumps and their turbulence.

Table 1 presents a summary of the properties of the clumps and the observational results discussed in this work. As well as the positions of the sources, it gives the clump sizes and surface densities (PI) and the non-thermal component of the 1D velocity dispersions of the N_2H^+ emission. The table also lists the Mach number of these non-thermal motions, and the virial parameter of the clumps.

The clump radius R was determined from the 2D Gaussian fit of the clump dust emission at 250 μm . The clump mass is estimated with a single-temperature grey-body fit of the source fluxes at 160, 250, 350 and 500 μm from Hi-GAL and, when available, including fluxes at 870 μm from the ATLASGAL (Schuller et al. 2009) maps and at 1.1 mm from the Bolocam Galactic Plane Survey (Aguirre et al. 2011) maps. The mass surface density, Σ , has been evaluated within the region defined by the clump radius (PI).

Since all the clumps are resolved in the N_2H^+ observations, the 1D velocity dispersion, σ_{obs} , has been determined using the CLASS task `hshf` to fit the hyperfine structure of the N_2H^+ spectra, averaged across all the pixels within the clumps. The non-thermal motions σ_{nth} are estimated as $\sigma_{\text{nth}} = (\sigma_{\text{obs}}^2 - \sigma_{\text{th}}^2)^{1/2}$, where σ_{th} is the thermal component of the velocity dispersion, $\sigma_{\text{th}} = (k_B T_{\text{kin}} / (\mu_{\text{N}_2\text{H}^+} m_{\text{H}}))^{1/2}$, where k_B is the Boltzmann constant, m_{H} the hydrogen mass and $\mu_{\text{N}_2\text{H}^+}$ the mean molecular weight ($\mu_{\text{N}_2\text{H}^+} = 29.02$). The gas kinetic temperature T_{kin} is fixed for each clump and equal to 10 K, comparable to the average dust temperature of these clumps ($\sim 11.2 \text{ K}$, PI). This leads to $\sigma_{\text{th}} \cong 0.05 \text{ km s}^{-1}$. Since the average non-thermal motion of the clumps is $\sigma_{\text{nth}} \cong 0.8 \text{ km s}^{-1}$, the contribution of the thermal velocity dispersion to σ_{obs} is minimal. Despite the fact that a temperature gradient of up to $\cong 10 \text{ K}$ can be expected across starless clumps (Peretto et al. 2010; Wilcock et al. 2012), using $T = 20 \text{ K}$ affects our results by less than 1 per cent. The Mach number \mathcal{M} is evaluated as $\sigma_{\text{nth}, 3\text{D}}/c_s$, with $\sigma_{\text{nth}, 3\text{D}} = \sqrt{3}\sigma_{\text{nth}}$ and $c_s = (k_B T_{\text{kin}} / (\mu_{\text{H}} m_{\text{H}}))^{1/2} \cong 0.19 \text{ km s}^{-1}$, with a mean molecular weight $\mu_{\text{H}} = 2.33$. We find $\mathcal{M} \geq 2$ for all the clumps, with an average value of $\overline{\mathcal{M}} = 7.54$.

3.2 Clump dynamics from HCO^+

To parametrize the asymmetry of the HCO^+ line, we calculate the parameter \mathcal{A}_{TG} as defined by equation (1), where $I(v_i)$ is the

Table 1. Clump properties. Column 1: name of the clumps as defined in PI. Columns 2 and 3: coordinates of the sources, defined as the peak identified in the dust 250 μm continuum maps. Column 4: radius of the clumps as defined by the dust continuum emission. Column 5: mass surface density derived from the FIR/sub-mm dust continuum emission. Column 6: non-thermal component of the 1D velocity dispersion. Column 7: Mach number. Column 8: virial parameter. Column 9: keyword to identify if the clump HCO^+ spectrum shows a symmetric or asymmetric profile based on the definition of the asymmetry parameter \mathcal{A}_{TG} as discussed in the text. Columns 10 and 11: measured \mathcal{A}_{TG} for both HCO^+ and HNC spectra, respectively.

Clump	RA (J2000) (hh: mm: ss)	Dec (J2000) (dd: mm: ss)	R (pc)	Σ (g cm^{-2})	σ_{nth} (km s^{-1})	\mathcal{M}	α_{vir}	HCO^+ spec.	$\mathcal{A}_{\text{TG}}(\text{HCO}^+)$	$\mathcal{A}_{\text{TG}}(\text{HNC})$
15.631−0.377	18:20:29.1	−15:31:26	0.54	0.06	0.30	2.68	0.21	Sym	0.11 ± 0.01	0.03 ± 0.01
18.787−0.286	18:26:15.3	−12:41:33	0.69	0.27	1.07	9.82	0.48	Asym	1.74 ± 0.23	0.91 ± 0.08
19.281−0.387	18:27:33.9	−12:18:17	0.67	0.10	0.47	4.28	0.25	Asym	0.80 ± 0.09	0.40 ± 0.04
22.53−0.192	18:32:59.7	−09:20:03	0.80	0.16	1.25	11.45	0.92	Asym	1.70 ± 0.12	1.21 ± 0.10
22.756−0.284	18:33:49.1	−09:13:04	0.55	0.14	0.95	8.68	0.88	Asym	1.80 ± 0.77	0.54 ± 0.08
23.271−0.263	18:34:38.0	−08:40:45	0.72	0.13	0.94	8.65	0.75	Asym	0.93 ± 0.10	0.63 ± 0.01
24.013+0.488	18:33:18.5	−07:42:23	0.81	0.20	0.91	8.33	0.40	Asym	1.15 ± 0.18	1.07 ± 0.15
25.609+0.228	18:37:10.6	−06:23:32	0.97	0.22	1.05	9.64	0.40	Asym	0.69 ± 0.14	0.36 ± 0.04
25.982−0.056	18:38:54.5	−06:12:31	0.80	0.09	0.69	6.31	0.50	Sym	0.27 ± 0.01	0.18 ± 0.01
28.178−0.091	18:43:02.7	−04:14:52	0.85	0.19	1.07	9.79	0.54	Asym	0.92 ± 0.25	0.04 ± 0.01
28.537−0.277	18:44:22.0	−04:01:40	0.67	0.17	0.78	7.16	0.41	Asym	0.43 ± 0.06	0.38 ± 0.03
28.792+0.141	18:43:08.8	−03:36:16	0.61	0.08	0.99	9.06	1.55	Sym	0.02 ± 0.01	0.00 ± 0.00
30.357−0.837	18:49:40.6	−02:39:45	0.67	0.06	0.57	5.19	0.68	Sym	0.14 ± 0.06	0.28 ± 0.07
31.946+0.076	18:49:22.2	−00:50:32	0.82	0.14	1.19	10.87	0.94	Asym	2.66 ± 0.27	0.43 ± 0.03
32.006−0.51	18:51:34.1	−01:03:24	0.70	0.06	0.31	2.85	0.18	Sym	0.20 ± 0.02	0.04 ± 0.01
34.131+0.075	18:53:21.5	+01:06:14	0.55	0.11	0.74	6.74	0.72	Asym	0.51 ± 0.16	0.21 ± 0.04

intensity at velocity v_i and $G(v_i)$ is the Gaussian fit to line, evaluated at velocity v_i . To restrict the comparison to the HCO^+ gas kinematically associated with dense gas traced by the N_2H^+ , the sum was carried out over a velocity range corresponding to ± 5 times the velocity dispersion of the N_2H^+ . This multiple was estimated by comparing the velocity widths of the N_2H^+ and HCO^+ emission, visual inspection of the spatial distribution of the HCO^+ as a function of velocity with the column density maps and comparison with a manual, source-by-source selection of the velocity range,

$$\mathcal{A}_{\text{TG}} = \frac{1}{A} \left(\sum_i |I(v_i) - G(v_i)| - B \right). \quad (1)$$

The quantity A is the peak intensity of the Gaussian fit to the HCO^+ line profile. This factor is necessary since the numerator of \mathcal{A}_{TG} is an integrated intensity, so that without the normalization, for two lines with the same intrinsic shape, the stronger line will have a larger value of \mathcal{A}_{TG} than the weaker line. The term in the summation represents the residual after the subtraction of the Gaussian fit to the original spectrum. Taking the modulus of the difference to measure the line asymmetry results in the noise in the spectrum producing a positive value for \mathcal{A}_{TG} , even for a symmetric line. To correct for this, a value B , the bias, is subtracted when calculating the line asymmetry. Since the value of B , the offset due to noise, depends on both the noise level in the spectrum and the velocity range over which the emission is detected, B was estimated for each source by summing the modulus of the noise over the same velocity width as the line asymmetry was determined, but centred at several different velocities away from the line.

Fig. 1 shows the asymmetry parameter with its uncertainties plotted against the clump surface density, Σ .

The value of \mathcal{A}_{TG} for each source is given in Table 1. Fig. 1 shows a strong correlation between the line asymmetry and the clump surface density, with high surface density regions having more asymmetric lines. This is confirmed by the Pearson correlation coefficient that gives a value of 0.55 for \mathcal{A}_{TG} with Σ , corresponding to a probability of 2.8×10^{-2} of the correlations being due to chance.

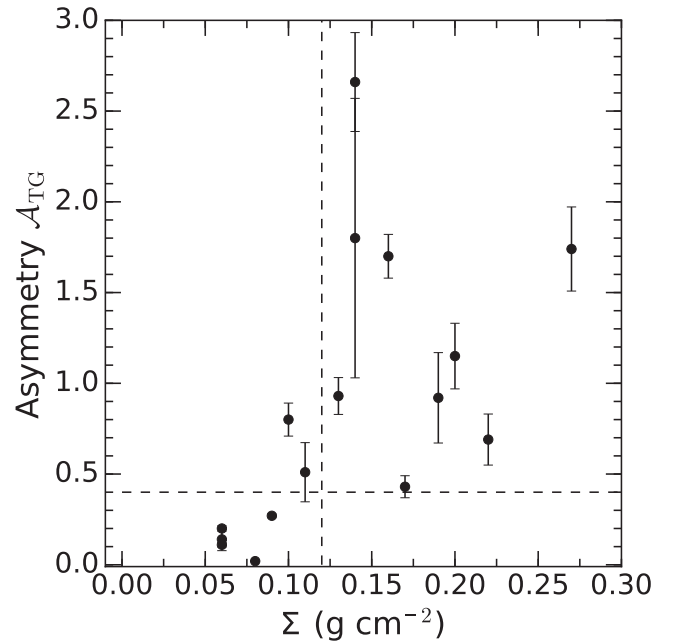


Figure 1. Asymmetry parameter, \mathcal{A}_{TG} , as a function of clump surface density, Σ . The horizontal dashed line indicates the value $\mathcal{A}_{\text{TG}} = 0.4$ that separates symmetric from asymmetric line profiles. The vertical dashed line delimits the surface density threshold $\Sigma = 0.12 \text{ g cm}^{-2}$, the value that maximizes the difference between more dynamically active clumps and the rest of the objects, as discussed in the text.

Clumps with $\mathcal{A}_{\text{TG}} < 0.4$ have a mean $\Sigma = 0.070 \pm 0.006 \text{ g cm}^{-2}$, while those with $\mathcal{A}_{\text{TG}} \geq 0.4$ have $\Sigma = 0.17 \pm 0.02 \text{ g cm}^{-2}$. An exact permutation test indicates that this has a probability of only 1.4×10^{-3} of being due to chance. For clumps below a surface density threshold $\Sigma_t = 0.12 \text{ g cm}^{-2}$, the mean value of $\mathcal{A}_{\text{TG}} = 0.3 \pm 0.1$ while clumps with $\Sigma_t \gtrsim 0.12 \text{ g cm}^{-2}$ have a mean $\mathcal{A}_{\text{TG}} = 1.3 \pm 0.2$, a difference that an exact random permutation test indicates has a probability of only 2×10^{-3} being due to chance. This threshold

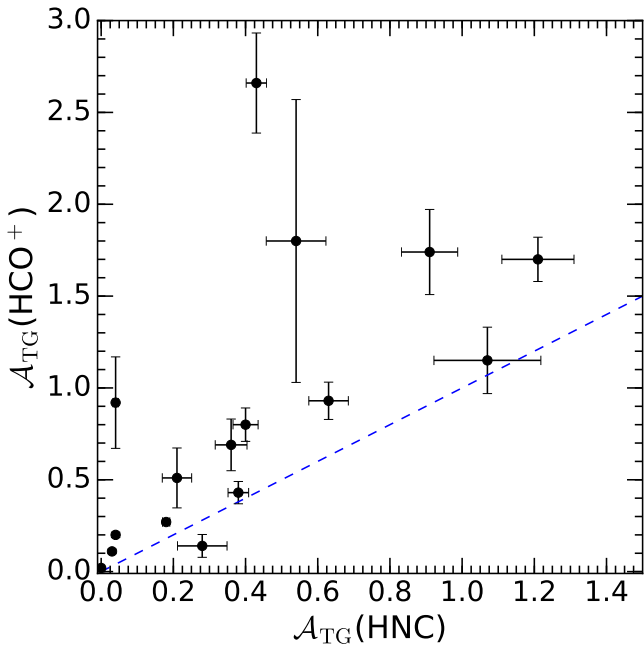


Figure 2. Comparison between $\mathcal{A}_{\text{TG}}(\text{HCO}^+)$ and $\mathcal{A}_{\text{TG}}(\text{HNC})$. The blue dashed line is the $y = x$ relation.

implies that all clumps above Σ_{t} have $\mathcal{A}_{\text{TG}} > 0.4$. Two clumps have $\Sigma \simeq 0.1 \text{ g cm}^{-2}$ and $\mathcal{A}_{\text{TG}} > 0.4$. Lowering the value of Σ_{t} to include them would lead to a difference between the two subsamples that an exact random permutation test indicates has a probability of 4×10^{-3} being due to chance, twice the probability obtained assuming $\Sigma_{\text{t}} = 0.12 \text{ g cm}^{-2}$. Therefore, we adopt $\Sigma_{\text{t}} = 0.12 \text{ g cm}^{-2}$ as the threshold that maximizes the difference between the two groups of clumps. For convenience, we label (in Table 1) sources with $\mathcal{A}_{\text{TG}} \geq 0.4$ as having asymmetric lines (more dynamically active) and the others as having symmetric lines. The HCO^+ line profiles are showed in PI.

The same analysis was also performed for the HNC (1–0) spectra. As Fig. 2 shows, there is a correlation between $\mathcal{A}_{\text{TG}}(\text{HCO}^+)$ and $\mathcal{A}_{\text{TG}}(\text{HNC})$ with a Pearson correlation coefficient of 0.63. In addition, the figure shows that for all but one of the sources the HCO^+ line is more asymmetric than the HNC line. Comparing the $\mathcal{A}_{\text{TG}}(\text{HNC})$ with the clump surface density shows similar results to the HCO^+ but with somewhat lower statistical significance that is consistent with the evidence from Fig. 2 that the HNC (1–0) transition is a somewhat poorer tracer of the clump dynamics. This is also consistent with the comparison of the linewidth of the HCO^+ (1–0) and HNC (1–0) (Fig. 3), which shows that the HCO^+ lines are typically broader than the HNC lines. A higher line broadening is a signpost of higher non-thermal motions, which may be due to a high level of turbulence and/or a significant dynamical activity, such as infall motions at the core and clump scales or outflows at the core scales (e.g. Lopez-Sepulcre, Cesaroni & Walmsley 2010; Smith et al. 2013; Palau et al. 2015). Chira et al. (2014) suggested that in some circumstances asymmetric line profiles in low- J transitions of optically thick lines such as HCO^+ (1–0) may also be interpreted as obscuration by surrounding filaments. However, the emission from N_2H^+ (1–0), which is optically thin in most of these sources (PI), does not show the presence of the multiple, dense gas velocity components that would be expected in the case of the emission originating from overlapping structures. Therefore, we assume that the asymmetries we observe are due to ongoing dynamical

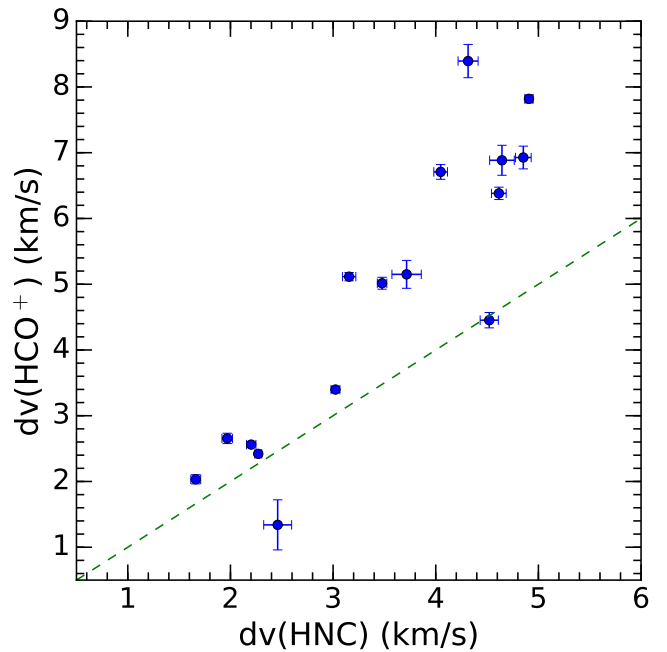


Figure 3. Comparison between HCO^+ and HNC linewidths. The green dashed line is the $y = x$ relation.

activity and the asymmetry–surface density correlation in HCO^+ (1–0), supported by the HNC (1–0) results, which show that high surface density clumps are more dynamically active than lower Σ clumps. In particular, the lack of symmetric lines towards high surface density clumps suggests that complex dynamics are intimately connected with the presence of the highest surface density regions.

4 A GRAVOTURBULENT DESCRIPTION OF THE STAR FORMATION PROCESS

4.1 Virial relation and force balance

4.1.1 Classical virial analysis

In the classical analysis of cloud stability, the non-thermal motions are due to local turbulence that supports the cloud. The dynamics of the collapse is described by two independent variables, the kinetic energy $E_k \propto \sigma^2$, where σ is the 1D observed (turbulent) velocity dispersion of the region, and the gravitational potential energy $E_G \propto M/R$, where M is the total mass within a region of radius R . The virial parameter α_{vir} describes the balance between these two energies, defined as (Bertoldi & McKee 1992)

$$\alpha_{\text{vir}} = a \frac{5\sigma^2 R}{GM} = 2a \frac{E_k}{E_G}, \quad (2)$$

where G is the gravitational constant and a is a constant that includes modifications due to non-spherical and inhomogeneous density distributions. Here we assume $a = 1$.

A critical value, α_{cr} , is defined as the value of α_{vir} for which the cloud is in equilibrium. If α_{vir} is greater than α_{cr} , the region will expand and dissolve; if it is lower, the region will collapse. In the absence of external pressure or magnetic fields, the hydrostatic equilibrium is reached when E_k is balanced by E_G and α_{vir} has a critical value $\alpha_{\text{cr}} = 1$ (Tan et al. 2014). If the region is under external pressure, this pressure will work towards compressing the cloud and therefore α_{cr} will increase. For instance, if clouds are

modelled as non-magnetized, pressure-bounded isothermal spheres, then they will be unstable and collapse if their mass is larger than the Bonnor–Ebert (BE) mass that leads to $\alpha_{\text{cr, BE}} \cong 2$ (see the discussion in Kauffmann et al. 2013; see also Tan et al. 2014). Conversely, in the presence of internal magnetic fields, the cloud can be stabilized against collapse and therefore α_{cr} decreases with respect to the non-magnetized case.

The virial parameter for our sources is systematically lower than 2, and for all but one source $\alpha_{\text{vir}} < 1$ ($28.792 + 0.141$, Table 1). The average value of α_{vir} is $\bar{\alpha}_{\text{vir}} \simeq 0.60$. This classical virial analysis would conclude that these clumps are all gravitationally bound.

A virial equilibrium state is a necessary condition in the turbulent core model of massive star formation (McKee & Tan 2003) on the assumption that in massive clumps the internal motions reflect turbulence and in the absence of magnetic fields (Tan et al. 2014).

Rather than being in a state of virial equilibrium, it is possible that in massive regions collapse occurs in a hierarchical, global fashion that itself generates non-thermal, gravoturbulent motion due to the chaotic collapse (Ballesteros-Paredes et al. 2011). In the simplest case with no external pressure or magnetic fields, the observed non-thermal motions would then arise from *both* local turbulence *and* self-gravity, and it is *not* independent from the gravitational term. This can be shown with a formulation of the problem in which the dynamics is described in terms of accelerations.

4.1.2 Describing the virial relation as accelerations

The quantity $a_G = \pi G \Sigma / 5$ describes the average gravitational acceleration of a region, and it is a function of the mass surface density $\Sigma = M / (\pi R^2)$ only. The kinetic term of the system is described by $a_k = \sigma^2 / R$, which also has the dimensions of an acceleration and is interpreted as the magnitude of the acceleration due to the total (thermal and non-thermal) motions in the region. If gravitational collapse significantly contributes to the observed linewidth, this would produce a correlation between a_G and a_k .

In this gravoturbulent scenario, a_k is proportional to a_G , and

$$\frac{a_k}{a_G} = \frac{\sigma^2}{R} \frac{5}{\pi G \Sigma} = \alpha_{\text{vir}} \implies a_k = \alpha_{\text{vir}} a_G \quad (3)$$

except, in this formulation, the interpretation of α_{vir} is substantially different. We cannot disentangle the turbulent from the gravitationally driven components in the observed a_k of each region. The measured gravoturbulent acceleration in a region with $\alpha_{\text{vir}} \leq 1$ could predominantly originate from either chaotic gravitational collapse or local turbulence supporting against the collapse, leading to two different star-forming scenarios (see Fig. 4). This ambiguity is particularly significant in GMCs and clumps. Similarly, in single cores, where the collapse is less chaotic, the contributions to a_k may be from the ordered motions due to the local collapse (and therefore the gravity) and from local turbulence, which are still indistinguishable. In the extreme case of all non-thermal motions being driven by self-gravity alone, $a_k = a_G$ and $\alpha_{\text{vir}} = 1$. Therefore, as long as the measured α_{vir} is lower than 2, a_G can still account for the majority of the observed non-thermal motions.

The advantage of this formulation however is the interpretation of the dynamics in a statistically significant sample of star-forming regions. If all the non-thermal motions in each region were to be gravitationally driven, then as the gravitational acceleration increases, one would expect a linear increase of the observed acceleration towards higher density regions. In a more realistic context, because gravity is not the only force in play, if observing regions at increasing surface densities (i.e. increasing a_G) we observe an increase

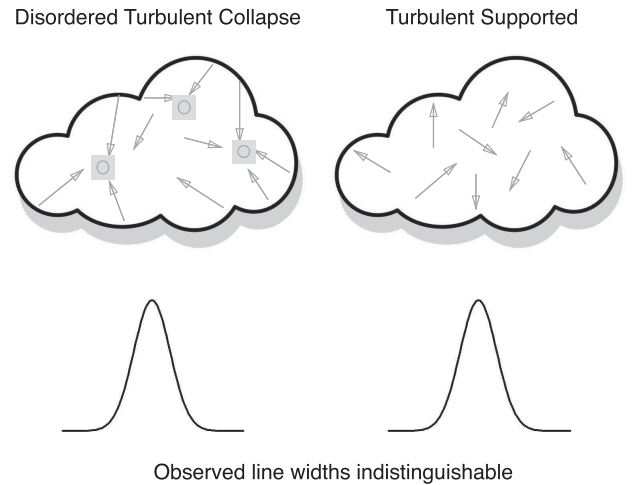


Figure 4. Cartoon of the self-gravity versus turbulence models. Top left: massive cloud with non-thermal motions generated only by the gravitational attraction of multiple centres of collapse. Top right: the same cloud with motions generated by random turbulence. Bottom: both self-gravity and turbulence generate non-thermal motions. The observed velocity dispersion (and the corresponding a_k) is the same and we cannot distinguish the origin of the non-thermal motions.

of a_k , it suggests that *on average* the majority of the non-thermal motions originate from gravitationally driven chaotic collapse, such that a_k is in fact a ‘gravoturbulent acceleration’.

The Heyer relation, which shows a strong indication of increasing $\sigma / R^{0.5}$ with increasing mass surface density, is equivalent to the a_k versus a_G relationship: the Heyer relationship is indeed equivalent to equation (3), by taking the square root of a_k and imposing $\alpha_{\text{vir}} = 1$. The Heyer relation correctly connects velocity dispersion, radius and surface density of the regions but has no direct physical interpretation of these quantities.

The Larson relation is a specific case of equation (3). For constant α_{vir} and constant Σ , equation (3) implies $\sigma \propto R^{0.5}$. In other words, when the gravitational acceleration is similar among different clouds, i.e. for similar values of the surface density of the clouds, and in condition of ‘virial equilibrium’ (whether for $\alpha_{\text{vir}} = 1$ or 2), then the acceleration in the system is fixed.

4.2 Implications for 70 μm quiet clumps

Fig. 5 shows the Heyer relation in the same units of the original H09 work, $\sigma / R^{0.5}$ and Σ , and in the a_k and a_G units. The clumps that show asymmetric HCO^+ spectra are indicated with red circles. The clumps follow an a_k versus a_G relationship and, in agreement with the discussion in Section 4.1, we interpret this trend as an indication that, on average, the non-thermal motions in these clumps may be mostly driven by self-gravity itself.

From Fig. 5, we can see that all the clumps with $\Sigma \geq 0.12 \text{ g cm}^{-2}$ show HCO^+ line asymmetries as defined in Section 3.2. All our clumps are also dominated by supersonic, non-thermal motions (see Table 1). The average Mach number \mathcal{M} of the clumps with $\Sigma \geq \Sigma_t$ is $\simeq 67$ per cent higher on average than the corresponding Mach number of the less dense clumps. These results also suggest that $\Sigma_t = 0.12 \text{ g cm}^{-2}$ could be seen as a threshold above which clumps show more evident signs of dynamical activity, perhaps indicative of gravitational collapse at clump scales.

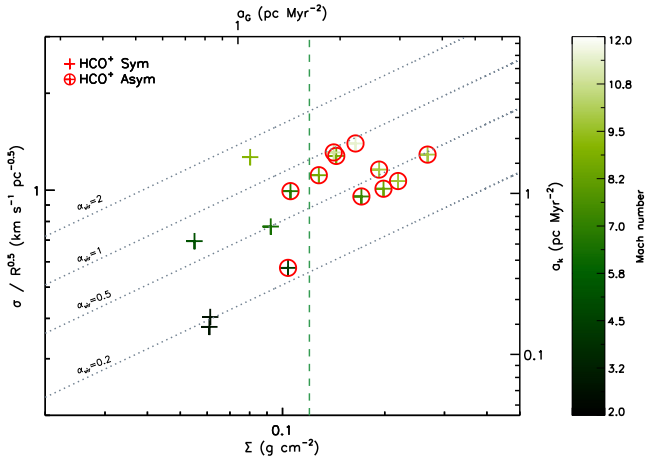


Figure 5. Heyer diagram for our 70 μm quiet clumps. Clumps are colour-coded with respect to the value of the respective Mach number. Also in this and the following figures, we show axes in acceleration units. Clumps for which the HCO^+ spectrum is asymmetric ($A_{\text{TG}} > 0.4$) are shown as circled plus signs. All of the clumps with $a_G \geq 1.6 \text{ pc Myr}^{-2} \cong 0.12 \text{ g cm}^{-2}$ (the green dotted line) show signs of dynamical activity. The grey dotted lines follow the loci of points for constant values of the virial parameter.

5 GRAVITATIONALLY DRIVEN a_k AT ALL SCALES?

5.1 From GMCs to cores

To explore the kinematics of the clumps in the context of both their environment (GMCs) and substructures (clumps and cores), in Fig. 6 we plot the a_k versus a_G relation (top panel) and the dependence of the virial parameter with the surface density (bottom panel). We consider data from the literature for three different loci of points (GMCs, massive clumps and massive cores at different evolutionary stages), as follows.

(1) The large, relatively low density GMCs traced with ^{13}CO occupy the left-hand side of the diagram. The points show the GMC data of the cloud as a whole (size 10–100 pc) discussed in H09. The clouds span a range of masses and surface densities of $2 \lesssim M \lesssim 2 \times 10^6 M_\odot$ and $2 \times 10^{-3} \lesssim \Sigma \lesssim 5 \times 10^{-2} \text{ g cm}^{-2}$, respectively (H09).

(2) The central region of the diagram is occupied by our massive clumps and the sample of massive clumps analysed in Gibson et al. (2009, size 0.6–4.0 pc, mass $200 \lesssim M \lesssim 2.5 \times 10^3 M_\odot$ and surface density $8 \times 10^{-3} \lesssim \Sigma \lesssim 6 \text{ g cm}^{-2}$) selected to be dark at 8 μm and observed with CS emission line, a tracer of dense gas in star-forming regions. This data set, combined with the H09 data, was used in Ballesteros-Paredes et al. (2011) to discuss their global collapse model.

(3) The right-hand side includes core-scale regions from different surveys, focusing on young pre-stellar and proto-stellar cores. The brown points are dense cores (size 0.03–0.05 pc, mass $3 \lesssim M \lesssim 40 M_\odot$ and surface density $0.6 \lesssim \Sigma \lesssim 6.8 \text{ g cm}^{-2}$) embedded in the massive clumps NGC 2264 C and D observed by Peretto, Andre & Belloche (2006). The surface density of each core has been derived from the size and mass in table 2 of Peretto et al. (2006). We used the data for the 11 resolved cores with a well-defined core radius. These clumps are located in the Mon OB-1 molecular cloud complex at $d \simeq 800 \text{ pc}$, and here we refer to the results from the N_2H^+ (1–0) data obtained with IRAM 30 m. The blue circles are pre-protoclusters (size 0.04–0.4 pc, mass $20 \lesssim M \lesssim 1.2 \times 10^3 M_\odot$

and surface density $5 \times 10^{-2} \lesssim \Sigma \lesssim 5 \text{ g cm}^{-2}$) observed with NH_2D in G29.960.02 and G35.201.74 (W48) by Pillai et al. (2011) using the Plateau de Bure Interferometer. Finally, the cyan crossed circles are a sample of 13 evolved cores (size 0.1 pc, mass $9 \lesssim M \lesssim 69 M_\odot$ and surface density $0.2 \lesssim \Sigma \lesssim 1.8 \text{ g cm}^{-2}$) observed in NH_3 (1–1) with the Very Large Array by Palau et al. (2015). We estimated the mass surface density assuming the core masses in table 1 of Palau et al. (2015) and assuming a fixed core radius as described in Palau et al. (2015).

From the top panel of Fig. 6, it is evident that, globally, a_k consistently increases with increasing a_G . One consequence of this result is that the first Larson relation, $\sigma \propto R^{0.5}$, is inconsistent from GMC to core scales. In Fig. 7, we show the σ against R relations for these surveys, overlaid with the Heyer & Brunt (2004) relation $\sigma \propto R^{0.56}$. The surveys together do not follow a $\sigma \propto R^{0.5}$ relation, and in particular, massive clumps and cores have similar non-thermal motions at all scales in the range $0.01 \lesssim R \lesssim 2 \text{ pc}$. Also, there is no clear global trend of the virial parameters from clouds to cores. To emphasize this, in the bottom panel of Fig. 6, we show GMCs, clumps and cores in the α_{vir} versus Σ plane. The green dotted vertical line indicates the $\Sigma_{\text{t}} = 0.12 \text{ g cm}^{-2}$ surface density threshold. Clouds and cloud fragments span a wide range of α_{vir} at all scales, and there is no evident distinction in the α_{vir} versus Σ plane below and above Σ_{t} .

If we focus on GMCs alone, there is a large dispersion in the a_k versus a_G plane, and the a_k and a_G relation is less obvious. Indeed, GMCs have a reasonably good Pearson correlation coefficient (0.47) in the σ versus R diagram in Fig. 7. The average virial parameter for the GMC sample is $\alpha_{\text{GMC}} = 1.9$ (H09) with many clouds having $\alpha_{\text{GMC}} > 2$ (see also Fig. 6, bottom panel). This value is higher than the average value of α_{vir} found in our clumps and in massive young cores as discussed in the next paragraphs. With the classical virial analysis, this would mean that the majority of the clouds are unbound on large scales. A possible explanation could be that the masses of GMCs are underestimated by a factor of 2–3 due to the local thermodynamic equilibrium approximation and the assumption of constant CO abundance (H09). Otherwise, this could instead be due to a high level of turbulence in the clouds that could lead to their dispersal in the absence of a confining pressure due to H I envelope.

Alternatively, in the description of the virial parameter as a ratio of accelerations, the high values of α_{vir} for GMCs imply that most of the non-thermal motions cannot be solely accounted for by the gravitationally driven acceleration. One possible explanation is that the external pressure acts as an additional confining force that contributes to the observed a_k (e.g. Field, Blackman & Keto 2011). In Section 5.2, we discuss the implications of accounting for an external pressure.

At clump scales, both surveys plotted in Fig. 6 (top panel) show an increase of a_k with a_G . Since the parameters in each survey have been estimated using different approaches, we fitted the samples of each survey separately. To do this, we used the `linfitex` IDL routine accounting for errors in both the estimation of a_k and a_G . We consider an error of 30 percent in the estimation of the mass surface density (i.e. a_G) and an error of 20 percent in the velocity dispersion and radius (i.e. a_k) estimations. The results of the best linear fit to each survey in the log-log space are shown as straight lines in the top panel of Fig. 6. The slopes are $A_{\text{clumps}} = 0.78 \pm 0.39$ and $A_{\text{Gib}} = 0.65 \pm 0.11$ for our clumps and the Gibson et al. (2009) clumps, respectively. Noticeably, these values are only slightly higher but still compatible with a slope of 0.5,

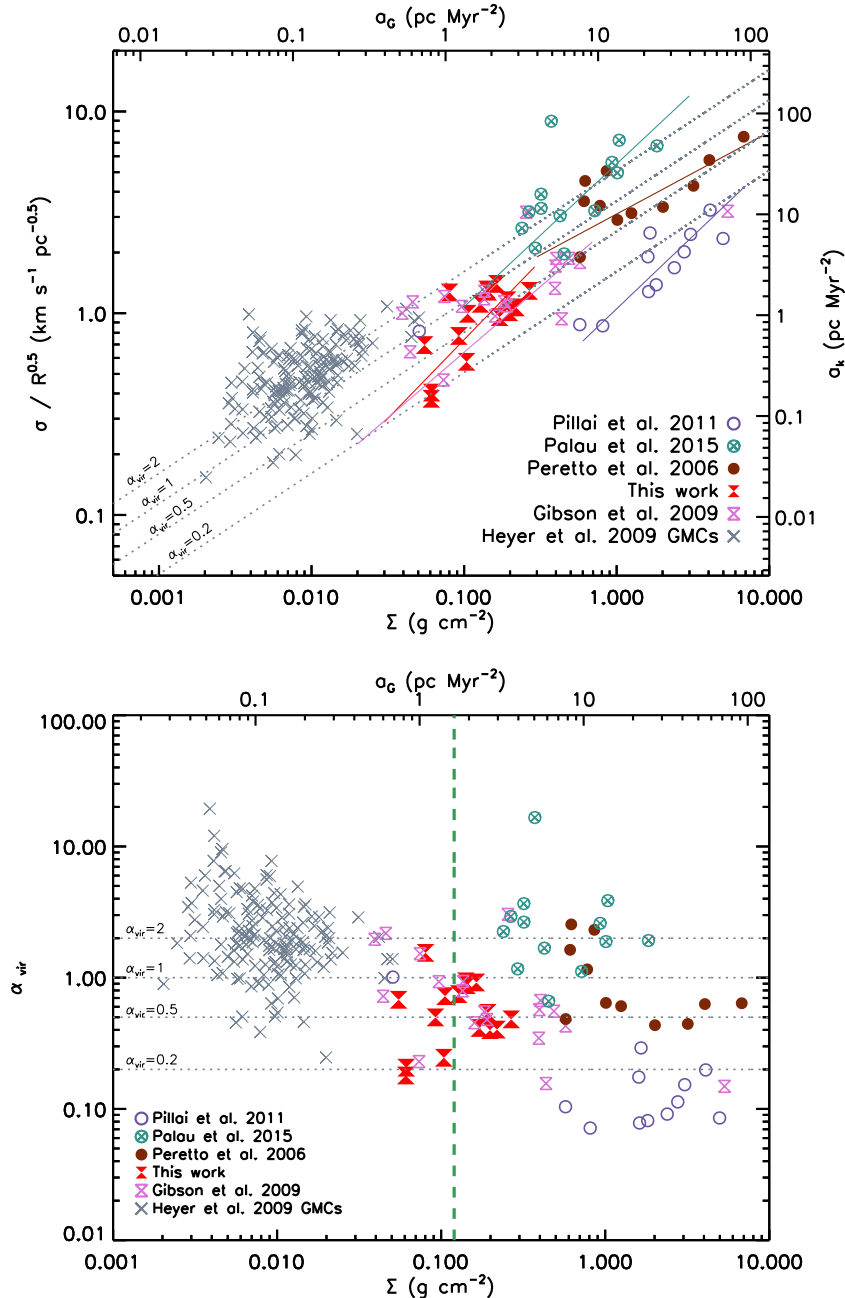


Figure 6. Top: a_k versus a_G relation described in equation (3). The red hourglass signs are our clumps. The grey crosses are the GMC values described in H09. The light purple hourglasses are the massive clumps identified by Gibson et al. (2009). The brown filled circles are the pre- and proto-stellar cores identified in NGC 2264 by Peretto et al. (2006). The cyan crossed circles are the massive proto-stellar cores described in Palau et al. (2015). Finally, the blue circles are massive cores observed by Pillai et al. (2011). The dotted lines show constant values of the virial parameter. Bottom: virial parameter as a function of the gravitational acceleration for the same objects as in the top panel. The green dotted line delimits the $\Sigma \geq 0.12 \text{ g cm}^{-2}$ region. The grey dotted lines show constant values of α_{vir} .

which would correspond to the expected slope in case of constant value of the virial parameter going towards regions of higher surface density, i.e. a linear increase of a_k at increasing a_G .

At core scales, the samples of Pillai et al. (2011) and Peretto et al. (2006), tracing massive pre-stellar and proto-stellar cores, lie mostly below $\alpha_{\text{vir}} = 1$, which is similar to what we find for our clumps (Fig. 6). The fits to these samples are also shown in the top panel of that figure, with slopes of $A_{\text{Pil.}} = 0.72 \pm 0.09$ and $A_{\text{Per.}} = 0.41 \pm 0.11$, respectively, broadly consistent with an increasing gravoturbulent acceleration towards regions of higher

surface densities. The sample of more evolved cores from Palau et al. (2015) lies close to or above $\alpha_{\text{vir}} = 2$. Although this means that most of the non-thermal motions cannot be accounted for by gravity alone, we still observe an increase of a_k with a_G with a slope of $A_{\text{Pal.}} = 0.71 \pm 0.17$, similar to what is observed in the samples of younger cores. The increased linewidth in these more evolved cores could perhaps be due to the local injection of turbulence from outflows (Sánchez-Monge et al. 2013; Palau et al. 2015).

A caveat of this analysis comes from the fact that each survey has its own systematics and methodology, making a direct comparison

between surveys difficult. For instance, different tracers may look at distinct regions along the line of sight and the estimated value of the linewidth (and therefore α_{vir}) for clouds or cloud fragments in each survey may be significantly affected by the chosen tracer (e.g. Palau et al. 2015).

Furthermore, in the analysis above, we have only considered the contribution of the gravitational acceleration to the total motions of a given region. Other forces can contribute to the non-thermal motions we observe, such as external pressure or magnetic fields. We explore the effect of these forces in Sections 5.2 and 5.3, respectively.

5.2 External pressure

In Galaxy-scale simulations and observations of nearby galaxies, GMCs have been found to have high values of α_{vir} , which would suggest that clouds are not gravitationally bound at tens of parsec scales (Dobbs, Burkert & Pringle 2011; Duarte-Cabral & Dobbs 2016). It has been suggested that these clouds could be under the effect of the external ram pressure from galactic motions and the thermal pressure of the surrounding hot ISM (e.g. Duarte-Cabral et al., in preparation), an idea consistent with the observations of nearby galaxies (Hughes et al. 2013).

If clouds are under an external pressure, equation (3) must be modified to account for the pressure contribution to the observed non-thermal motion. In the standard virial analysis, the pressure term can be added to equation (3) as (Field et al. 2011)

$$\frac{\sigma^2}{R} = \alpha_{\text{vir}} \frac{\pi G \Sigma}{5} + \frac{4P_{\text{ext}}}{3\Sigma}. \quad (4)$$

In the acceleration formulation, equation (4) becomes

$$a_k = \alpha_{\text{vir}} a_G + \frac{4\pi G}{15} \frac{P_{\text{ext}}}{a_G} \equiv \hat{\alpha}_{\text{vir}}(a_G) a_G, \quad (5)$$

with

$$\hat{\alpha}_{\text{vir}}(a_G) = \alpha_{\text{vir}} \left(1 + \frac{4\pi G}{15\alpha_{\text{vir}}} \frac{P_{\text{ext}}}{a_G^2} \right). \quad (6)$$

Equation (5) implies that a_k will not be proportional to only the gravitational acceleration where the external pressure dominates and when the gravitational acceleration is sufficiently low. Equation (6) shows that the virial parameter $\hat{\alpha}_{\text{vir}}$ of a pressure-confined cloud (or cloud fragment) is greater than α_{vir} . For large values of a_G , the terms $\propto P_{\text{ext}}/a_G^2$ in equation (5) go rapidly to zero and $\hat{\alpha}_{\text{vir}} \rightarrow \alpha_{\text{vir}}$.

The theoretical value of the external pressure generated by the neutral ISM and required to confine a molecular cloud is of the order of $P_{\text{ext}}/k \simeq 10^4 \text{ K cm}^{-3}$ (Elmegreen 1989). Observations of individual regions show a range of values, from $P_{\text{ext}}/k = 5 \times 10^4 \text{ K cm}^{-3}$ (Bertoldi & McKee 1992) to $P_{\text{ext}}/k = 5 \times 10^5 \text{ K cm}^{-3}$ in nearby starless cores (Belloche et al. 2011).

In Fig. 8, we show the same data points of Fig. 6, this time including the loci of points occupied by the solution of equation (5) for two different values of external pressure, $P_{\text{ext}}/k = 10^4$ and 10^5 K cm^{-3} (the solid and the dot-dashed line, respectively), and for various values of α_{vir} . The figure shows that with a contribution of an external pressure of e.g. $P_{\text{ext}}/k = 10^4 \text{ K cm}^{-3}$ at $a_G \lesssim 0.65 \text{ pc Myr}^{-2}$, a_k is mostly driven by the external pressure. For a cloud with $\Sigma = 0.01 \text{ g cm}^{-2} \equiv a_G = 0.13 \text{ pc Myr}^{-2}$ and, in the absence of external pressure, $\alpha_{\text{vir}} = 0.5$, the corresponding acceleration will be $a_k \simeq 0.066 \text{ pc Myr}^{-2}$. If we include a contribution of an external pressure of $P_{\text{ext}}/k = 10^5 \text{ K cm}^{-3}$, we will measure

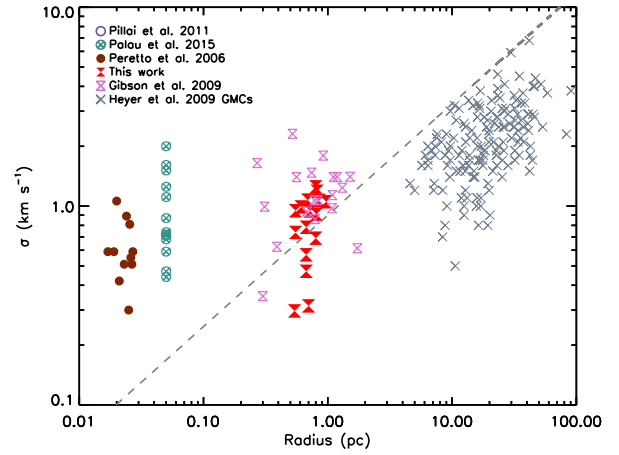


Figure 7. Velocity dispersion against radius relation. Symbols are the same as Fig. 6. Grey dotted line is the Larson relation as found by Heyer & Brunt (2004): $\sigma \propto R^{0.56}$. The cores in the survey of Palau et al. (2015) have radius fixed to $R = 0.05 \text{ pc}$.

$a_k \simeq 0.67 \text{ pc Myr}^{-2}$ and $\hat{\alpha}_{\text{vir}} \simeq 4.9$. The high values of the virial parameter observed in GMCs can therefore be explained by motions induced by an external pressure. At $a_G \geq 0.65 \text{ pc Myr}^{-2}$, gravity starts to dominate and the kinetic acceleration increases again with increasing gravitational acceleration at all scales, from GMCs down to cores, consistent with the threshold discussed in McKee, Li & Klein (2010) and Tan et al. (2014).

We conclude that with typical values of external pressure in the ISM, most of the observed a_k in GMCs can be driven by external pressure, with a negligible contribution of the gravitational acceleration. However, at some point, the gas surface densities will increase to high enough values such that gravity can take over at driving the majority of the non-thermal motions, effectively acting as a gravoturbulent acceleration.

5.3 Magnetic fields

Magnetic fields can also act as a large-scale support against gravity (Bertoldi & McKee 1992; Tan et al. 2013).

In the classical virial analysis, for the magnetic fields to act as support against gravitational collapse of a hydrostatic isothermal sphere, we obtain (Kauffmann et al. 2013)

$$B_{\text{eq}} = 81 \mu\text{G} \frac{M_\Phi}{M_{\text{BE}}} \left(\frac{\sigma_{\text{N}_2\text{H}^+}}{\text{km s}^{-1}} \right)^2 \left(\frac{R}{\text{pc}} \right)^{-1}, \quad (7)$$

where M_Φ is the magnetic flux mass for a field of mean strength $\langle B_{\text{eq}} \rangle$ (Tomisaka, Ikeuchi & Nakamura 1988), M_{BE} the Bonnor-Ebert mass and $M_\Phi/M_{\text{BE}} \simeq 2/\alpha_{\text{vir}} - 1$ (Kauffmann et al. 2013).

Observationally, Crutcher (2012) suggested, however, that there is an upper limit of the intensity of the magnetic field B_{up} in a given region that depends on the gas number density, as $B_{\text{up}} \simeq 150 \mu\text{G} (n_{\text{H}_2}/10^4 \text{ cm}^{-3})^{0.65}$. If we assume a spherical geometry and a density equal to the mean density, B_{up} can be rewritten as (Kauffmann et al. 2013)

$$B_{\text{up}} \simeq 336 \mu\text{G} \left(\frac{M}{10 M_\odot} \right)^{0.65} \left(\frac{R}{0.1 \text{ pc}} \right)^{-1.95}. \quad (8)$$

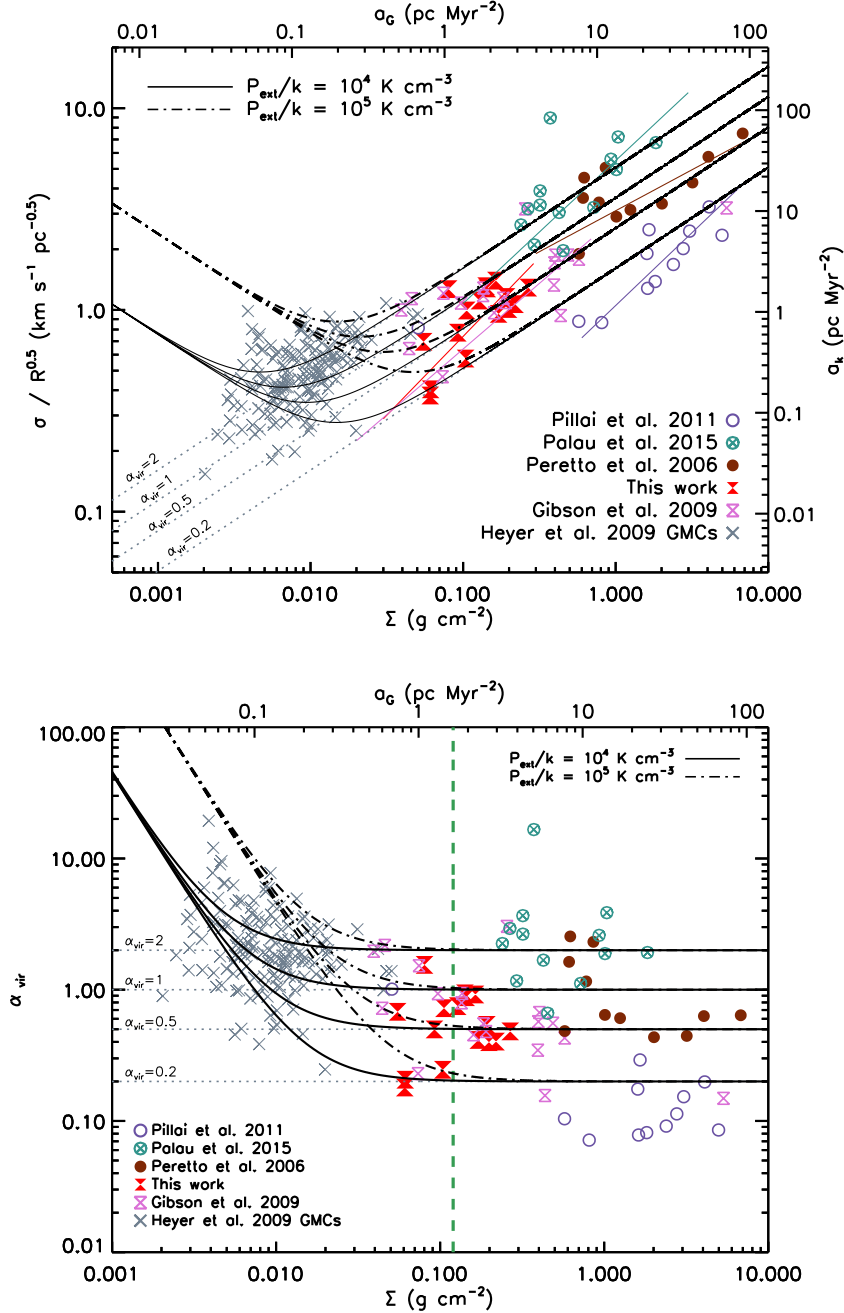


Figure 8. Same as Fig. 6, including the solutions of equation (5) for two different values of the external pressure and for fixed values of α_{vir} .

We can then compare the strength of the magnetic fields required to reach the virial equilibrium (that is, $B = B_{\text{eq}}$) with the critical value B_{up} . In Table 2, we report B_{eq} , B_{up} and the ratio between the two for our sample, where we separate the clumps above and below the surface density threshold for clarity.

In Fig. 9, we show the ratio $B_{\text{eq}}/B_{\text{up}}$ as a function of Σ . There is a good correlation between $B_{\text{eq}}/B_{\text{up}}$ and Σ (Pearson’s coefficient $\rho = 0.69$, which implies a probability of a non-correlation of only 0.003). This implies that for larger Σ , the magnetic fields needed to prevent collapse are increasingly greater than the maximum values predicted by Crutcher (2012), and therefore they cannot halt collapse.

In the framework of accelerations, we can instead look at how the magnetic fields could generate a negative acceleration that opposes gravity, preventing the collapse. If we take B_{up} from equation

(8) as an upper limit for the strength of the magnetic fields in our clumps, we can estimate the maximum magnetic pressure as $P_{B_{\text{up}}} = B_{\text{up}}^2 / (8\pi)$ and therefore derive the maximum magnetic acceleration, $a_{B_{\text{up}}}$, as

$$a_{B_{\text{up}}} = \frac{F_{B_{\text{up}}}}{M} = \frac{P_{B_{\text{up}}} \pi R^2}{M} \rightarrow a_{B_{\text{up}}} = \frac{B_{\text{up}}^2}{8\pi \Sigma}. \quad (9)$$

In Fig. 10, we compare $a_{B_{\text{up}}}$ with the acceleration imposed by the gravitational potential of the clumps, a_G . The figure shows that, above a surface density of $\Sigma \simeq 0.18 \text{ g cm}^{-2}$, the maximum acceleration generated by the magnetic fields is not sufficient to overcome a_G and therefore the collapse will proceed. Nevertheless, we observe signs of dynamical activity in clumps with $\Sigma < 0.18 \text{ g cm}^{-2}$, even though they have $a_G/a_{B_{\text{up}}} < 1$.

Table 2. Magnetic field estimates for clumps above and below the surface density threshold $\Sigma = 0.12 \text{ g cm}^{-2}$. Column 1: name of the clumps. Column 2: keyword to identify clumps that show symmetric (Sym) or asymmetric (Asym) HCO⁺ spectra. Column 3: intensity of the magnetic field required to reach BE equilibrium, B_{eq} . Column 4: maximum intensity of the magnetic field as estimated following Crutcher (2012), B_{up} . Ratio between B_{eq} and B_{up} .

Clump	Type	B_{eq} (μG)	B_{up} (μG)	$\frac{B_{\text{eq}}}{B_{\text{up}}}$
18.787–0.286	Asym	337	211	1.6
19.281–0.387	Asym	186	129	1.4
22.53–0.192	Asym	197	161	1.2
22.756–0.284	Asym	150	175	0.9
23.271–0.263	Asym	189	151	1.2
24.013+0.488	Asym	342	177	1.9
25.609+0.228	Asym	260	141	1.8
28.178–0.091	Asym	376	188	2.0
28.537–0.277	Asym	324	195	1.7
31.946+0.076	Asym	158	140	1.1
34.131+0.075	Asym	124	141	0.9
15.631–0.377	Sym	108	100	1.1
25.982–0.056	Sym	145	108	1.3
28.792+0.141	Sym	40	117	0.3
30.357–0.837	Sym	104	93	1.1
32.006–0.51	Sym	120	92	1.3

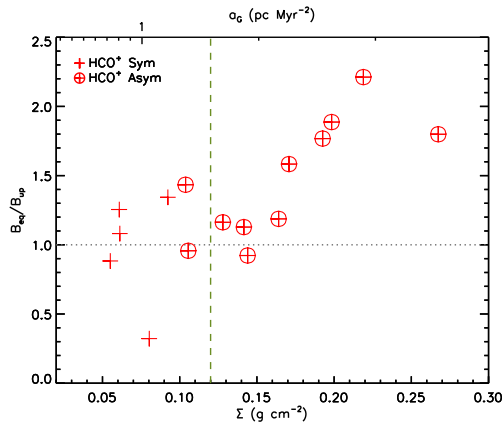


Figure 9. Ratio $B_{\text{eq}}/B_{\text{up}}$ as a function of the gravitational acceleration (i.e. surface density) of each clump. The correlation is significant with a Pearson coefficient of 0.69. All but four clumps have $B_{\text{eq}}/B_{\text{up}} \geq 1$ (the dotted horizontal line), i.e. they need an intensity of the magnetic field higher than the maximum allowed as predicted by Crutcher (2012). The green dashed vertical line marks the value $\Sigma_t = 0.12 \text{ g cm}^{-2}$.

This could be due to the fact that $a_{B_{\text{up}}}$ is a strict upper limit to the magnetic acceleration. In fact, not only it assumes the maximum value of the magnetic fields from Crutcher (2012), but it also considers the geometry of the magnetic fields such that all the gas would feel the same resistance due to the magnetic force. For instance, in a case of a uniform magnetic field threading the clump, only the gas trying to collapse perpendicular to the field lines would feel this maximum tension.

6 CONCLUSIONS

We have used new IRAM 30 m observations of a sample of 16 70- μm quiet clumps identified in IRDCs in the Hi-GAL survey

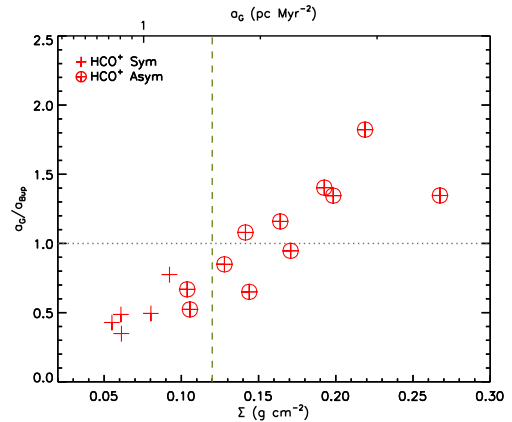


Figure 10. Same as Fig. 9, but for the ratio of the gravitational acceleration a_G to the maximum acceleration produced by magnetic fields a_B . The black dotted horizontal line is in correspondence of $a_G/a_{\text{up}} = 1$. The green dashed vertical line marks the value $\Sigma_t = 0.12 \text{ g cm}^{-2}$.

to explore the kinematics of these regions. The clumps have been selected to be ‘quiescent’, i.e. dark or very faint at 70 μm and with an $L/M < 0.3$ (PI). With these data, we show that there is a correlation between the asymmetry of the HCO⁺ line profile, tracing the dynamics of the regions, and the clump surface density, with the highest surface density clumps having the most asymmetric lines, and so being the most dynamically active.

Looking at the relationship between column density, size and velocity dispersion, we demonstrate that the Heyer relation can be re-interpreted as a direct consequence of a gravoturbulent description of the non-thermal motions in collapsing clouds and cloud fragments. In this formalism, the virial parameter is described as a ratio between the gravitational acceleration a_G and the observed acceleration a_k , the former defined as a function of the mass surface density and the latter as a function of the velocity dispersion and the radius of the cloud or cloud fragment.

We have used our sample of 16 massive 70 μm quiet clumps to explore this formalism, together with other surveys of GMCs, clumps and pre- and proto-stellar cores from the literature.

We can summarize our findings as follows.

(1) The non-thermal motions observed in clouds and cloud fragments originate from both self-gravity and turbulence that can act against gravity itself. The two components cannot be observationally separated. However, the data show that, from the scales of clumps (and possibly GMCs) down to the cores, the global measured acceleration, a_k , increases with the gravitational acceleration, a_G . This suggests that, on average, the self-gravity can drive much of the observed non-thermal motions at all spatial scales.

(2) For our sample of massive 70 μm quiet clumps, we find asymmetric line profiles tracing dynamical activity, which we interpret as due to gravitational collapse, regardless of the estimated value of α_{vir} in the single regions, suggesting that the virial parameter is not a good descriptor of the stability of a region. In our formulation, in the absence of magnetic fields and external pressure, α_{vir} can instead be seen as a measure of how much the non-thermal motions can be generated by gravity. Indeed, as long as $\alpha_{\text{vir}} < 2$ ($a_k < 2a_G$), gravity can dominate the non-thermal motions. This is the case for all our clumps, which would be consistent with them all being dynamically active and undergoing collapse.

(3) From our data, we identify a surface density value, $\Sigma_t \simeq 0.12 \text{ g cm}^{-2}$, above which all our clumps have highly

asymmetric HNC and HCO⁺ spectra, which we interpret as tracing collapse. We interpret this as the threshold above which gravity is strong enough to dominate the non-thermal motions at clump scales. In a scenario in which massive protostars accrete dynamically from their parent clump, Σ_c could therefore represent the minimum surface density at clump scales for high-mass star formation to occur.

(4) An external pressure P_{ext} that confines the GMCs such that $P_{\text{ext}}/k \simeq 10^4\text{--}10^5 \text{ K cm}^{-3}$ explains the high values of the measured non-thermal motions observed in these clouds, and does not exclude that the majority of them are globally collapsing. The contribution of the external pressure can be incorporated in the formalism of the gravoturbulent mechanism, modifying the definition of α_{vir} .

(5) Magnetic fields, if present, can be a support against the collapse. From the classical view, we show that magnetic fields stronger than the maximum intensity of the magnetic field suggested by Crutcher (2012) would be required to support the majority of the clumps. A similar conclusion can be drawn by comparing the gravitational acceleration to the maximum acceleration produced by the magnetic fields.

The gravoturbulent formulation and the a_k versus a_G relation, if confirmed at all scales, may help our understanding of the massive star formation mechanism. If the global collapse mechanism with the gravity driving much of the non-thermal motions is correct, and the strength of the magnetic fields is not sufficient, we may for example expect to observe pure thermal Jeans fragmentation in most of the clumps. This hypothesis can be explored using high-resolution instruments such as NOEMA or ALMA.

ACKNOWLEDGEMENTS

This work has benefited from research funding from the European Community's Seventh Framework Programme. AT and GAF are supported by STFC consolidated grant ST/L000768/1 to JBCA. RJS gratefully acknowledges support from the STFC through an Ernest Rutherford Fellowship. AT wants to thank J. Ballesteros-Paredes and E. Vázquez-Semadeni for their inspiring works and S. Camera for the stimulating conversations at the origin of this work.

REFERENCES

Aguirre J. E. et al., 2011, *ApJS*, 192, 4
 Ballesteros-Paredes J., Hartmann L. W., Vázquez-Semadeni E., Heitsch F., Zamora-Avilés M. A., 2011, *MNRAS*, 411, 65
 Belloche A. et al., 2011, *A&A*, 527, A145
 Bertoldi F., McKee C. F., 1992, *ApJ*, 395, 140
 Chira R. A., Smith R. J., Klessen R. S., Stutz A. M., Shetty R., 2014, *MNRAS*, 444, 874
 Crutcher R. M., 2012, *ARA&A*, 50, 29

Dobbs C. L., Burkert A., Pringle J. E., 2011, *MNRAS*, 413, 2935
 Duarte-Cabral A., Dobbs C. L., 2016, *MNRAS*, 458, 3667
 Elmegreen B. G., 1989, *ApJ*, 338, 178
 Field G. B., Blackman E. G., Keto E. R., 2008, *MNRAS*, 385, 181
 Field G. B., Blackman E. G., Keto E. R., 2011, *MNRAS*, 416, 710
 Fuller G. A., Myers P. C., 1992, *ApJ*, 384, 523
 Gibson D., Plume R., Bergin E., Ragan S., Evans N., 2009, *ApJ*, 705, 123
 Heyer M. H., Brunt C. M., 2004, *ApJ*, 615, L45
 Heyer M. H., Krawczyk C., Duval J., Jackson J. M., 2009, *ApJ*, 699, 1092 (H09)
 Hughes A. et al., 2013, *ApJ*, 779, 46
 Ibáñez-Mejía J. C., Mac Low M.-M., Klessen R. S., Baczynski C., 2016, *ApJ*, 824, 41
 Jackson J. M. et al., 2006, *ApJS*, 163, 145
 Kauffmann J., Pillai T., Goldsmith P. F., 2013, *ApJ*, 779, 185
 Krumholz M. R., Tan J. C., 2007, *ApJ*, 654, 304
 Larson R. B., 1981, *MNRAS*, 194, 809
 Lopez-Sepulcre A., Cesaroni R., Walmsley C. M., 2010, *A&A*, 517, A66
 McKee C. F., Ostriker E. C., 2007, *ARA&A*, 45, 565
 McKee C. F., Tan J. C., 2003, *ApJ*, 585, 850
 McKee C. F., Li P. S., Klein R. I., 2010, *ApJ*, 720, 1612
 Padoan P., Nordlund Å., 2002, *ApJ*, 576, 870
 Palau A. et al., 2015, *MNRAS*, 453, 3785
 Peretto N., Andre P., Belloche A., 2006, *A&A*, 445, 979
 Peretto N. et al., 2010, *A&A*, 518, L98
 Pillai T., Kauffmann J., Wyrowski F., Hatchell J., Gibb A. G., Thompson M. A., 2011, *A&A*, 530, A118
 Sánchez-Monge Á. et al., 2013, *MNRAS*, 432, 3288
 Schuller F. et al., 2009, *A&A*, 504, 415
 Smith R. J., Shetty R., Beuther H., Klessen R. S., Bonnell I. A., 2013, *ApJ*, 771, 24
 Solomon P. M., Rivolo A. R., Barrett J., Yahil A., 1987, *ApJ*, 319, 730
 Tan J. C., Kong S., Butler M. J., Caselli P., Fontani F., 2013, *ApJ*, 779, 96
 Tan J. C., Beltrán M. T., Caselli P., Fontani F., Fuente A., Krumholz M. R., McKee C. F., Stolte A., 2014, in Beuther H., Klessen R. S., Dullemond C. P., Henning T., eds, *Protostars and Planets VI*. Univ. Arizona Press, Tucson, p. 149
 Tomisaka K., Ikeuchi S., Nakamura T., 1988, *ApJ*, 335, 239
 Traficante A., Fuller G. A., Peretto N., Pineda J. E., Molinari S., 2015, *MNRAS*, 451, 3089
 Traficante A., Fuller G. A., Billot N., Duarte-Cabral A., Merello M., Molinari S., Peretto N., Schisano E., 2017, *MNRAS*, 470, 3882 (PI)
 Urquhart J. S. et al., 2014, *MNRAS*, 443, 1555
 Vasyunina T., Linz H., Henning T., Zinchenko I., Beuther H., Voronkov M., 2011, *A&A*, 527, A88
 Vázquez-Semadeni E., Gómez G. C., Jappsen A.-K., Ballesteros-Paredes J., Klessen R. S., 2009, *ApJ*, 707, 1023
 Wilcock L. A. et al., 2012, *MNRAS*, 422, 1071

This paper has been typeset from a \LaTeX file prepared by the author.